



ELSEVIER

Physics of the Earth and Planetary Interiors 129 (2002) 245–264

PHYSICS
OF THE EARTH
AND PLANETARY
INTERIORS

www.elsevier.com/locate/pepi

Anomalies of temperature and iron in the uppermost mantle inferred from gravity data and tomographic models

Frédéric Deschamps^{a,*}, Jeannot Trampert^a, Roel Snieder^b

^a Department of Geophysics, Utrecht University, Budapestlaan 4, P.O. Box 80021, 3508 TA Utrecht, The Netherlands

^b Department of Geophysics, Colorado School of Mines, Golden, CO 80401, USA

Received 29 May 2001; received in revised form 9 October 2001; accepted 9 October 2001

Abstract

We propose a method to interpret seismic tomography in terms of thermal and compositional anomalies. In addition to the tomographic model, we use gravity data, which provide information on the density expressed as a relative density-to-shear wave velocity scaling factor ($\zeta = \partial \ln \rho / \partial \ln V_s$). The inferred values of ζ are not consistent with the presence of thermal anomalies alone. However, simultaneous anomalies of temperature and composition explain the observations. Compositional anomalies can have several origins, but we find the most relevant parameter to be the global volumic fraction of iron ($x_{\text{Fe}} = \text{Fe} / (\text{Fe} + \text{Mg})$). We invert the tomographic model S16RLBM (Woodhouse and Trampert, 1995) and the density anomalies correlated to V_s -anomalies ($\delta \rho / \rho_0 = \zeta \delta V_s / V_0$) for anomalies of temperature (δT) and iron (δFe). The partial derivatives are provided by a numerical method that reconstructs density and seismic velocity for given temperatures and petrologic models (Vacher et al., 1998). Down to $z = 300$ km depth, the distribution of temperature and iron anomalies strongly depends on the surface tectonics. The continental mantle below old cratons and stable platforms is colder than average and depleted in iron, whereas the oceanic mantle is mostly homogeneous. Due to uncertainties on the reference state of the mantle, error bars on δT and δFe reach 10% of the inverted values. Finally, we apply these results to the stability of continental roots and test the hypothesis that the negative buoyancy induced by lower than average temperatures is balanced by the positive buoyancy induced by the depletion in iron. We find that continental roots are stable only if the viscosity of the mantle is strongly temperature-dependent. However, some uncertainties remain on the real effects and importance of rheology. © 2002 Elsevier Science B.V. All rights reserved.

1. Introduction

The continent–ocean distribution is a major feature of the Earth's surface and it extends down to the Earth's shallow interior. Global and regional models of seismic tomography, including recent ones (e.g. Woodhouse and Trampert, 1995; Alsina et al., 1996; Su and Dziewonski, 1997; Mégnin and Romanowicz, 2000; Ritsema and van Heijst, 2000; Villaseñor et al., 2001), report high-velocity roots below continents

down to 200–400 km depth. These continental roots were first noted by Jordan (1975), and their origin is still a matter of debate. According to Jordan (1975), the uppermost mantle below continental shields is colder than the oceanic mantle and chemically less dense. Therefore, horizontal temperature gradients are stabilized by horizontal compositional gradients, and the mantle below continental shields is prevented from flowing. This stable layer is usually referred as the tectosphere. An alternative model involves a phase transition (Anderson, 1987): horizontal temperature variations induce variations in the depth at which phase transitions take place. For instance, if the mantle

* Corresponding author.

E-mail address: deschamp@geo.uu.nl (F. Deschamps).

is colder than average (e.g. in the slabs), the olivine \rightarrow β -spinel transition should occur at lower pressure, i.e. at depths shallower than in the rest of the mantle. However, further studies presented arguments for the presence of a stable and chemically distinct layer below cratons. Jordan (1988) reviewed geophysical arguments, including gravimetric and geothermic data, that agree with this hypothesis. Polet and Anderson (1995) pointed out that high-velocity anomaly roots could be explained by a depletion in iron and/or an enrichment in olivine. Doin et al. (1996) showed that a depleted peridotitic layer at the base of the continental lithosphere is consistent with the geoid at intermediate wavelengths (spherical harmonic degrees 6–30).

The difficulties raised by the interpretation of seismic data results from the fact that density and seismic velocities depend simultaneously on temperature, composition and pressure. The recent study by Goes et al. (2000) suggests that in the upper mantle seismic velocity are mostly sensitive to temperature. Numerical models that reconstruct seismic velocities (e.g. Davies and Dziewonski, 1975; Duffy and Anderson, 1989; Vacher et al., 1998) support this conclusion. Temperature variations induce strong relative V_s -anomalies, whereas variations in the volumic fraction of olivine and in the iron content do not (see Fig. 2 in Section 3). In other words, V_s -anomalies may be useful to constrain the temperature distribution, but they are not sufficient to determine the chemical variations, as suggested by Forte and Perry (2000). To infer chemical variations, one needs an additional set of data, such as density anomalies. Relative V_s -anomalies are converted in density anomalies using a scaling factor ζ :

$$\zeta(r, \theta, \varphi) \equiv \frac{\partial \ln \rho(r, \theta, \varphi)}{\partial \ln V_s(r, \theta, \varphi)} \quad (1)$$

Radial models of this scaling factor can be deduced from inversions of tomographic models and gravity data. Previous models (e.g. Kogan and McNutt, 1993; Forte et al., 1995) included strong a priori information about the shape and the amplitude of the function $\zeta(z)$. Forte et al. (1995) used gravity data up to the spherical harmonic degree $\ell = 8$ and concluded to the presence of internally stabilized continent–ocean chemical differences.

Using several geodynamic data sets and tomographic models, Forte and Perry (2000) have recently

mapped anomalies of temperature (δT) and iron (δFe) in the uppermost mantle. They showed that the tectosphere is depleted in iron. In this paper, we infer distributions of δT and δFe in the uppermost mantle ($z \leq 300$ km) following a similar method but using different gravity data set, tomographic model and radial model of scaling factor. We also use a refined numerical model to invert V_s -anomalies and density anomalies for δT and δFe . Our results are in good agreement with Forte and Perry (2000), and we use them to study the stability of continental roots.

2. Scaling factor in the uppermost mantle

Fig. 1 represents the sub-continental and sub-oceanic scaling factor deduced from inversions of gravity data and tomographic model (Deschamps et al., 2001). Linear inversions were performed separately for continental and oceanic areas, according to the equation

$$\delta g(\theta, \varphi) = \int_{r_{\text{CMB}}}^R K(r, \theta, \varphi) \zeta(r) dr, \quad (2)$$

where the gravity anomalies (δg) and the S-wave velocity anomalies (δV_s) are filtered out between spherical harmonic degrees ℓ_1 to ℓ_2 :

$$\delta g(\theta, \varphi) = \sum_{\ell=\ell_1}^{\ell_2} \delta g_\ell(\theta, \varphi), \quad (3)$$

$$K(r, \theta, \varphi) = \frac{3\rho_0(r)g_0}{\bar{\rho}R} \times \sum_{\ell=\ell_1}^{\ell_2} \left[\frac{(\ell-1)}{2\ell+1} G_\ell(r) \frac{(\delta V_s)_\ell(r, \theta, \varphi)}{V_0(r)} \right]. \quad (4)$$

In these equations R is the Earth's radius, $\bar{\rho}$ is the mean density, g_0 is the surface acceleration of gravity, and $\rho_0(r)$ and $V_0(r)$ the reference density and S-wave velocity models. In Fig. 1 the reference model is PREM (Dziewonski and Anderson, 1981), the gravity anomalies are the non-hydrostatic gravity anomalies derived from the geoid model EGM96 (Lemoine et al., 1998), and the S-wave anomalies are provided by the global tomographic model S16RLBM (Woodhouse and Trampert, 1995), which is expanded up to the spherical harmonic degree $\ell = 16$. Each degree of the

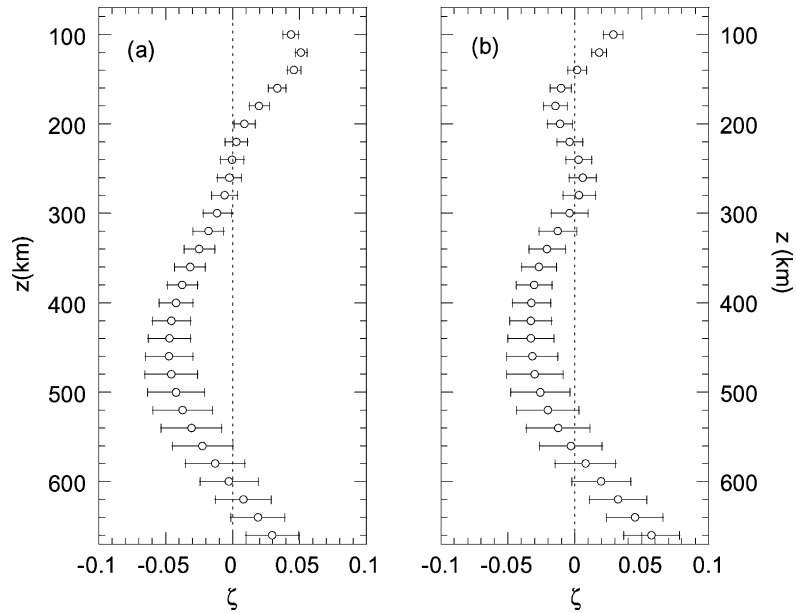


Fig. 1. Inverted scaling factor (ζ) in the sub-continental (a) and sub-oceanic (b) upper mantle. Open circles indicate the mean value of ζ , and the error bars represent the variance in ζ . The variance was estimated by introducing randomly generated errors in the seismological model S16RLBM. Data are filtered for degrees $\ell = 11$ –16, integration (2) is performed from $z = 1000$ km depth up to the surface, and the viscosity model is MF2 (Mitrovia and Forte, 1997).

V_s -anomalies expansion is weighted by a geoid kernel $G_\ell(r)$, that is to say the geoid response to an anomaly of density located at radius r . These functions account for mantle dynamics, and therefore, they depend on the radial viscosity model (Forte and Peltier, 1991). To obtain the models of ζ presented in Fig. 1, we used a recent viscosity model proposed by Mitrovia and Forte (1997), which was built to fit both the long-wavelength gravity anomalies and the relaxation time due to postglacial uplift. One may point out that this choice is arbitrary. However, others viscosity models lead to similar results, suggesting that down to $z = 400$ km $\zeta(z)$ does not depend on the viscosity profile (Deschamps et al., 2001). For degrees $\ell \geq 11$ the geoid kernels peak around $z = 200$ – 300 km and have negligible values from $z = 1000$ km down to the core–mantle boundary. Removing low degrees does not have a dramatic effect on the scaling factor in the uppermost mantle. The models of ζ obtained for degrees $\ell_1 = 2$ to $\ell_2 = 16$ are similar to those presented in Fig. 1, which were obtained by filtering the data between degrees $\ell_1 = 11$ and $\ell_2 = 16$. The spectral

window $11 \leq \ell \leq 16$ is, therefore, well suited to sample the shallow mantle ($100 \leq z \leq 400$ km). On the other hand, canceling the lowest degrees ($\ell = 2$ – 4) removes most of the seismic signal at depths greater than 400 km, and the scaling factors for $\ell = 2$ – 16 and $\ell = 11$ – 16 are significantly different. In addition, our model is poorly constrained at depths greater than 350 km. For these reasons, we have voluntarily limited the present study to depths shallower than 300 km. Sub-continental and sub-oceanic scaling factors are clearly different. Below continents (oceans), the scaling factor has positive values down to $z = 220$ km (140 km) depth. The order of magnitude is 0.04, which is small in comparison to the usual experimental mineralogy estimates. Compared to previous models (e.g. Kogan and McNutt, 1993; Forte et al., 1995), our results are significantly different in shape and amplitude. These studies have imposed strong a priori information to constrain the value of ζ . On the other hand, we did not assume any a priori information, except smoothness. Finally, if one accounts for anelasticity, our inverted model of ζ is in good agreement with

experimental mineralogy estimates. However, negative and low values of ζ cannot be explained by pure variations of temperature. Additional variations of composition are the most obvious choice to explain such values.

3. Synthetic anomalies of density and S-wave velocity

Previous studies have constructed numerical approaches to explain seismological models in terms of temperature and mineralogical composition (e.g. Davies and Dziewonski, 1975; Duffy and Anderson, 1989; Vacher et al., 1996). Such techniques reconstruct seismic velocities and densities using laboratory measurements of elastic and thermal properties of the main minerals present in the mantle rocks. Comparison with a globally averaged seismic model (e.g. PREM or ak135) provides good constraints on the value of the mantle adiabat (Vacher et al., 1996). On the other hand, the mineralogical composition, particularly the volume fraction of olivine (X_{ol}), have a limited influence on the seismic velocities. Duffy and Anderson (1989) preferred a piclogitic composition ($X_{ol} = 40\%$) for the transition zone. Using a more recent compilation of experimental data, Vacher et al. (1998) do not find significant differences between the pyrolitic ($X_{ol} = 61.7\%$) and piclogitic compositions down to 660 km. At 660 km depth, the presence of ilmenite could explain the observed discontinuity, but it does not matter whether ilmenite is present in pyrolite or in piclogite. Recently, Goes et al. (2000) have computed temperature variations from V_p - and V_s -anomalies beneath Europe down to 200 km depth. A conclusion is that compositional effects induce velocity anomalies smaller than 1% and would, therefore, be difficult to resolve.

Laboratory measurements of elastic data are usually performed at very high frequencies (around 1 MHz). Recently, Jackson (2000) measured the shear modulus for olivine at frequencies close to those of the seismic waves. At temperatures higher than 900 °C, the values of the shear modulus at 0.01 and 0.3 Hz differ significantly from those at 1 MHz. This discrepancy is attributed to anelasticity, which is also responsible for attenuation in the Earth's mantle. Karato (1993) showed that if one does not account for anelasticity,

the temperature anomalies deduced from V_s -anomalies are overestimated. Therefore, synthetic seismic velocities computed from elastic data at 1 MHz should incorporate anelastic effects. Velocities that account for anelasticity are usually expressed in terms of the quality factor Q (Minster and Anderson, 1981):

$$V_{\text{anel}} = V_{\text{elast}} \left[1 - \frac{1}{2Q(\omega, p, T) \tan(\pi a/2)} \right] \quad (5)$$

where a is a constant, ω the frequency of the seismic wave, p the pressure and T is the temperature. Anderson and Given (1982) proposed that attenuation results from thermally and volumetrically activated process, and that the quality factor can be expressed by

$$Q(\omega, p, T) = A\omega^a \exp \left[\frac{a(H + pV_a)}{RT} \right] \quad (6)$$

where A is a constant, H the activation enthalpy, p the pressure, V_a the volume of activation and R is the gas constant. Goes et al. (2000) used this formulation and proposed two possible models for Q . Their model Q_1 , based on data by Sobolev et al. (1996) fits well the absorption band model of Anderson and Given (1982). In this paper, we computed relative anomalies of density and S-wave velocity, as a function of temperature and compositional anomalies. Anomalies are calculated with respect to the reference density and velocity obtained for a reference temperature, mineralogical composition, and iron content. Velocities and densities are computed along adiabatic profiles of temperature following the method of Vacher et al. (1998) (this method is outlined in the Appendix A). We accounted for anelastic effects using Eqs. (5) and (6), and the model Q_1 of Goes et al. (2000) that is to say $A = 1.48 \times 10^{-1}$, $a = 0.15$, $H = 500$ kJ/mol and $V_a = 20$ cm³/mol. Most of the following calculations were performed for a frequency $f = 0.1$ Hz. Before turning to the inverse problem, we first consider two illustrations of the direct problem.

First, we have computed relative V_s -anomalies ($\delta V_s/V_0$, plain line in Fig. 2) and density anomalies ($\delta\rho/\rho_0$, dashed line in Fig. 2) as a function of variations of temperature (δT), global volumic fraction of iron (δFe) and volumic fraction of olivine (δX_{ol}) with respect to a reference model. The global volumic fraction of iron (or iron ratio) is defined by the ratio $x_{\text{Fe}} = \text{Fe}/(\text{Fe} + \text{Mg})$ of the bulk rock. In Fig. 2, the reference temperature and global iron ratio are equal

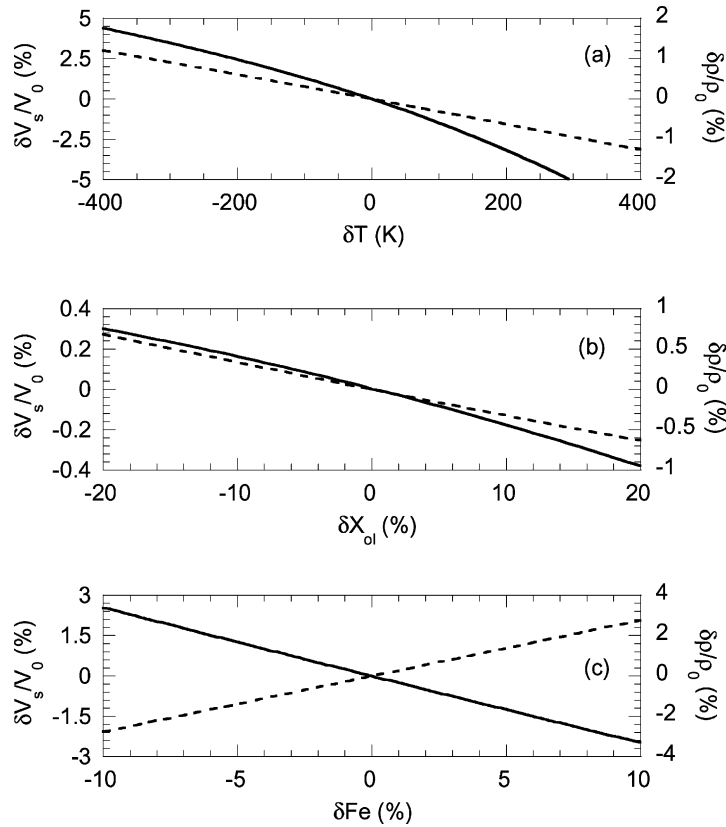


Fig. 2. Relative anomalies of S-wave velocity ($\delta V_s/V_0$, solid curve) and density ($d\rho/\rho_0$, dashed curve) as a function of anomalies of temperature (a), anomalies of the volumic fraction of olivine (b), and anomalies of the global volumic fraction of iron (c). The reference temperature, olivine fraction and iron ratio are $T_{ref} = 1250^\circ\text{C}$, $X_{ol,ref} = 61.7\%$ (pyrolite) and $x_{Fe,ref} = 11\%$. Anelasticity is accounted for according to the model Q_1 of Goes et al. (2000), and assuming $f = 0.1$ Hz.

to 1250°C and 11%, respectively and the reference mineralogical composition is pyrolite. In pyrolite the volumic fraction of olivine is $X_{ol} = 61.7\%$, and the non-olivine components (with their volumic fraction) are clinopyroxene (13.3%), orthopyroxene (5.2%), garnet (15.3%) and jadeite (4.5%). The deficit/excess of olivine is shared between the non-olivine minerals as a function of their volumic fraction in the reference composition. For instance, if the rock is depleted in olivine by 10%, the composition of the rock is as follows: olivine 51.7%, clinopyroxene 16.8%, orthopyroxene 6.5%, garnet 19.3% and jadeite 5.7%. It is clear that $\delta V_s/V_0$ is much more sensitive to temperature variations than to mineralogical variations (Fig. 2a and b). If all the deficit/excess in olivine is put in garnet, variations of velocity are more important.

However, garnet is richer in iron than the other minerals, and most of the variations are due to the global enrichment/depletion in iron associated with the enrichment/depletion in garnet. The influence of the global iron ratio is stronger than that of the olivine fraction, but it remains weak compared to that of temperature. A velocity anomaly equal to 1% requires an iron anomaly of -4% . The same anomaly can be obtained with a temperature anomaly of -50 K only. The distribution of V_s -anomalies should, therefore, impose relatively strong constraints on the distribution of temperature. Compositional changes, on the other hand, cannot be inferred from V_s -anomalies alone. One needs an additional data set, such as density anomalies. Indeed, the sensitivity of density anomalies to temperature and chemical variations are comparable

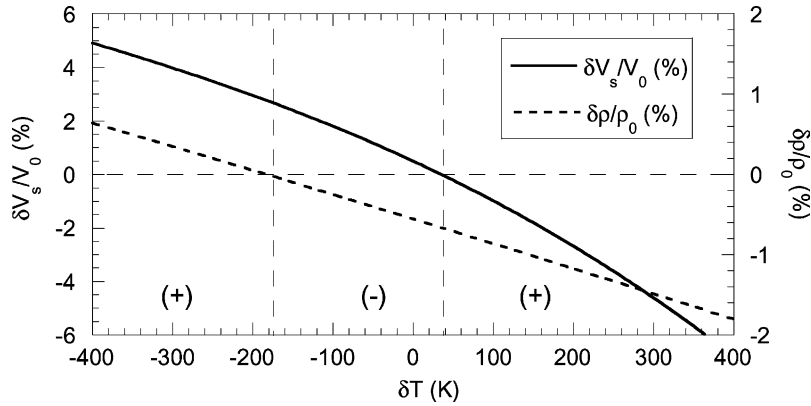


Fig. 3. Relative density anomalies (dashed line) and V_s -anomalies (solid line) as a function of temperature anomalies and for a depletion in iron equal to -2% . The reference temperature, olivine fraction and iron ratio are $T_{\text{ref}} = 1250^\circ\text{C}$, $X_{\text{ol,ref}} = 61.7\%$ (pyrolite) and $x_{\text{Fe,ref}} = 11\%$. The scaling factor is negative for temperature between -180 and $+20$ K, and positive elsewhere. The correction for anelasticity is the same than in Fig. 2.

(dashed curves in Fig. 2). Note that the iron content has a strong influence on density anomalies. For instance, a depletion in iron of 2% induces the same density anomaly than an increase of temperature of 180 K or than an enrichment in olivine of 17% .

The second example gives a key to interpret the negative and low values of the scaling factor. The density and the seismic velocity are both decreasing (increasing) as the temperature is increasing (decreasing). In the case of purely thermal anomalies the scaling factor is, therefore, always positive, and its typical value (if one accounts for anelasticity) is around 0.2 . On the other hand, if the rock is enriched (depleted) in iron, V_s decreases (increases) whereas ρ increases (decreases). For pure anomalies of iron, the scaling factor is always negative, and it has values around -1.1 . If one considers simultaneous variations of temperature and iron, it is, therefore, possible that the scaling factor attains values smaller than 0.1 and even that it even is negative. Fig. 3 shows relative anomalies of density ($\delta\rho/\rho_0$, dashed curve) and S-wave velocity ($\delta V_s/V_0$, plain curve) as a function of temperature variations, assuming an iron depletion of 2% (that is to say the global volumic fraction of iron is equal to 9% instead of 11%). Relative anomalies of ρ and V_s cancel for $\delta T \sim 20$ K and $\delta T \sim -180$ K, respectively. As a result, there is a wide range of temperature anomalies for which the scaling factor yields negative values. To interpret our estimated scaling

factor (and, therefore, the gravity data and the tomographic model) one must account for simultaneous variations of temperature and composition.

4. Inverse problem

4.1. Method

We have used the method outlined in the previous section as a basis to invert the relative V_s -anomalies and the density anomalies correlated to these V_s -anomalies ($\delta\rho/\rho_0 = \zeta \delta V_s/V_0$) for variations of temperature and composition. First, we write the variations of the quantity Y_i relatively to a reference value $Y_{i,\text{ref}}$ as a function of the variations in the parameters X_j relatively to a reference value $X_{j,\text{ref}}$:

$$\frac{\delta Y_i}{Y_{i,\text{ref}}} = \sum_j a_{ij} \delta X_j; \quad a_{ij} = \frac{\delta Y_i}{Y_{i,\text{ref}} \delta X_j} \quad (7)$$

To compute the coefficients a_{ij} , we used the approach of Vacher et al. (1998) (Appendix A). Since these coefficients depend on the δX_j , we linearized the system. The process is initiated by imposing a priori starting values of δX_j . At iteration n , the δX_j^n determined at the previous iteration are used to compute the coefficients a_{ij} . Eq. (7) can easily be inverted for estimated values of δX_j^n . These estimated values provide in turn

estimated values of δY_i (δX_j^n). The residues $R_i^n = \delta_i - \delta Y_i^n$ are then used to compute updated values of δX_j (δX_j^{n+1}), following a Newton–Raphson method. This process is stopped when the residues are small enough.

Since we have two sets of parameters ($\delta V_s/V_0$ and ζ), we have access to the variations of two parameters only. In this paper, we focus on anomalies of temperature (δT) and global iron molar fraction (δFe). In that case, one must solve the system:

$$\begin{cases} \frac{\delta V_s}{V_0} = A \delta T + \delta \text{Fe} \\ \frac{\delta V_s}{V_0} = C \delta T + D \delta \text{Fe} \end{cases} \quad (8)$$

where $A = \delta V_s/(V_0 \delta T)$, $B = \delta V_s/(V_0 \delta \text{Fe})$, $C = \delta \rho/(\rho_0 \delta T)$ and $D = \delta \rho/(\rho_0 \delta \text{Fe})$. The choice to invert for anomalies of iron rather than for anomalies of olivine is driven by the observation that densities and seismic velocities are more sensitive to global iron content than to olivine fraction (Fig. 2b and c). Usual values of the velocity anomalies require large anomalies of olivine. For instance, if $\delta V_s/V_0 = 2\%$ the rock is enriched in olivine by 7–14%, depending on the value of ζ . Such anomalies may not be relevant to the case of the Earth's uppermost mantle. In addition, pure anomalies of olivine induce a positive scaling factor (density and velocity are both decreasing as X_{ol} is increasing, Fig. 2c), and may not explain the negative values of the observed ζ .

Forte and Perry (2000) parameterized the chemical variations in terms of a garnet depleted basalt. This choice was driven by the observation that variations in alumina (Al_2O_3), which is preferentially stored in garnet, strongly influence the density and seismic velocities (e.g. Jordan, 1979). We did calculations that confirm this point: for instance, a depletion in garnet equal to 10% induce a V_s -anomaly of -1.2% and a density anomaly of -0.8% . Such anomalies are larger than those induced by variations in olivine, but they remain 3–4 times smaller than those induced by variations in iron. Note that the seismic velocity and the density both decrease as the volumic fraction of garnet decreases, i.e. the scaling factor associated with pure variations of garnet is positive. Accounting for depletion in garnet leads to larger temperature variations and smaller variations in iron. For instance, if one imposes a depletion of garnet of

5%, the anomalies of iron are only 70% of those for a rock undepleted in garnet. To infer garnet and iron variations simultaneously one needs an additional constraint, such as P-wave velocity anomalies. Taking $\partial \ln V_s / \partial \ln V_p = 1.6$ (Robertson and Woodhouse, 1997), and for $\delta V_s/V_0 = 4\%$, the depletion in garnet is close to 2%, and the anomalies of iron are about 90% of those obtained for pyrolite. Since pure variations in garnet fail to explain large velocity anomalies and a negative scaling factor, we chose to consider variations in the iron content only. This is, we believe, the most important effect, keeping in mind that the variations in iron we infer may be slightly overestimated.

4.2. Estimation of error bars

An important issue is to estimate error bars for δT and δFe . Of course, errors in $\delta V_s/V_0$ and in ζ propagate to δT and δFe . The errors on δT ($\sigma_{\delta T}$) and δFe ($\sigma_{\delta \text{Fe}}$) can be estimated by the quadratic sum of the errors on δV_s ($\sigma_{\delta V_s}$) and ζ (σ_{ζ}). After inverting the system (8), one obtains

$$\begin{cases} \sigma_{\delta T}^2 = \frac{(D - B\zeta)^2 \sigma_{\delta V_s}^2 + (B \delta V_s)^2 \sigma_{\zeta}^2}{(AD - BC)^2} \\ \sigma_{\delta \text{Fe}}^2 = \frac{(A\zeta - C)^2 \sigma_{\delta V_s}^2 + (A \delta V_s \sigma_{\zeta}^2)}{(AD - BC)^2} \end{cases} \quad (9)$$

For the sake of simplicity, we assumed that A , B , C and D do not depend on $\delta V_s/V_0$ and ζ . If one provides values for $\sigma_{\delta V_s}$ and σ_{ζ} , then $\sigma_{\delta T}$ and $\sigma_{\delta \text{Fe}}$ can be calculated during the inversion process (Section 4.1). We performed calculations for many different cases (with $-10\% \leq \delta V_s \leq 10\%$ and $-0.1 \leq \zeta \leq 0.1$), and found the relative errors on δV_s and ζ . For instance, if $\sigma_{\delta T}/\delta T = 10\%$ and $\sigma_{\zeta}/\zeta = 10\%$, Eq. (9) predict values of $\sigma_{\delta T}/\delta T$ and $\sigma_{\delta \text{Fe}}/\delta \text{Fe}$ close to 10%. The inversion propagates the errors, but does not amplify them. It is interesting to note that most of these errors (about 90%) are due to the error in δV_s . Unfortunately, tomographic models usually do not provide this uncertainty.

An additional source of error results from the choice of the model of reference, i.e. the temperature (T_{ref}), olivine fraction ($X_{\text{ol,ref}}$) and iron ratio ($x_{\text{Fe,ref}}$) used to compute the reference velocity and density. The inverted values of δT and δFe depend on these parameters. The thermodynamic reference model for

the Earth's mantle is, however, poorly constrained, which leads to uncertainties in δT and δFe . The most sensitive parameter is the reference temperature. The reference temperature can be seen as the potential temperature (i.e. temperature at zero pressure) of the mantle adiabat, and it should fit the average seismic models (such as PREM) reasonably well. The values of δT and δFe for $T_{\text{ref}} = 1000^\circ\text{C}$ and 1500°C differ by about 140 K and 1.4%, respectively. The reference olivine fraction is less sensitive than the reference temperature, but variations of δT and δFe with $X_{\text{ol,ref}}$ cannot be neglected. Variations in $x_{\text{Fe,ref}}$, on the other hand, do not induce significant differences in the values of δT and δFe . For instance, the values of δT and δFe for $x_{\text{Fe,ref}} = 5\%$ and $x_{\text{Fe,ref}} = 20\%$ differ by only 2 K and 0.02%, respectively. For these reasons, we have computed values of δT and δFe for all the values of T_{ref} and $X_{\text{ol,ref}}$ that provide values of V_s yielding within $\pm 2.5\%$ of the PREM value. As a result, we obtained mean distributions of δT and δFe as a function of $\delta V_s/V_0$ and ζ , together with their variances $\sigma_{\delta T}$ and $\sigma_{\delta Fe}$. These variances give an estimation of the error bars on δT and δFe . For depths between $z = 100$ and 300 km, error bars on δT (δFe) are equal to about 7% (10%) of the inverted values.

The distributions of δT and δFe presented hereafter (Sections 4.3 and 4.4) are the mean of a collection of distributions obtained for different values of T_{ref} and $X_{\text{ol,ref}}$, as explained above. Since variations in the reference iron ratio induce only small errors, we kept the value of $x_{\text{Fe,ref}}$ constant and equal to 11%. A reasonable estimate of the error due to the uncertainty on T_{ref} and $X_{\text{ol,ref}}$ is about 7–10% of the inverted values. This mean error may increase slightly if one also considers errors due to uncertainties on δV_s and ζ (Eq. (9)).

4.3. Simultaneous variations of temperature and iron

To illustrate the method presented in Section 4.1, we first consider simultaneous variations of temperature and global iron content as a function of $\delta V_s/V_0$ and ζ (Fig. 4). Positive (negative) anomalies of V_s are associated with negative (positive) anomalies of temperature and iron depletion (enrichment). Anelasticity effects, and therefore, the sensitivity of V_s to temperature

variations, are increasing with temperature (Eqs. (5) and (6)). As a result, temperature anomalies are getting stronger (in absolute value) as $\delta V_s/V_0$ is increasing (Fig. 4a). For instance, if $\zeta = 0.05$ the anomalies of temperature predicted by relative V_s -anomalies of -4 and 4% are equal to 175 and -230 K, respectively. Anomalies of iron, and to a lesser extent, anomalies of temperature, are sensitive to the scaling factor. For a given value of $\delta V_s/V_0$, the anomaly of iron is getting stronger as ζ is decreasing (Fig. 4b).

The inverted anomalies of temperature and iron are both correlated to the V_s -anomalies, and are, therefore, correlated one another. This is a consequence of the definition of the scaling factor Eq. (1), which implies that density anomalies are correlated to the V_s -anomalies. Eq. (8), however, are independent (the determinant $AD - BC$ is not equal to 0), and the inverted δT and δFe are two different results. The role of the scaling factor is to get correct amplitudes of density anomalies through gravity anomalies, keeping the spatial variations correlated to the V_s -anomalies.

The method presented in this study provides the anomalies of temperature and iron that are correlated to the V_s -anomalies. Indeed, our model of $\zeta(z)$ does not explain the observed gravity anomalies (δg) completely (Deschamps et al., 2001), and some additional anomalies of temperature and iron, which are not correlated to the velocity, must be present. Presently, we do not have access to these anomalies. However, the gravity anomalies predicted by our model of $\zeta(z)$ yield within $\pm 2s_{\delta g}$ of the observed gravity anomalies (Deschamps et al., 2001), suggesting that most of the density anomalies are correlated to the velocity anomalies. The distributions of δT and δFe for the Earth's mantle proposed in the next section are, therefore, robust features.

4.4. Application to the uppermost mantle

We now invert relative V_s -anomalies and the density anomalies correlated to V_s -anomalies for three-dimensional distributions of temperature and iron anomalies in the uppermost mantle. The input data are the spherical harmonic degrees $\ell = 2$ –16 of the global S-wave model S16RLBM (Woodhouse and Trampert, 1995), and the radial model of scaling factor proposed by Deschamps et al. (2001). We have computed a collection of distributions of δT and δFe

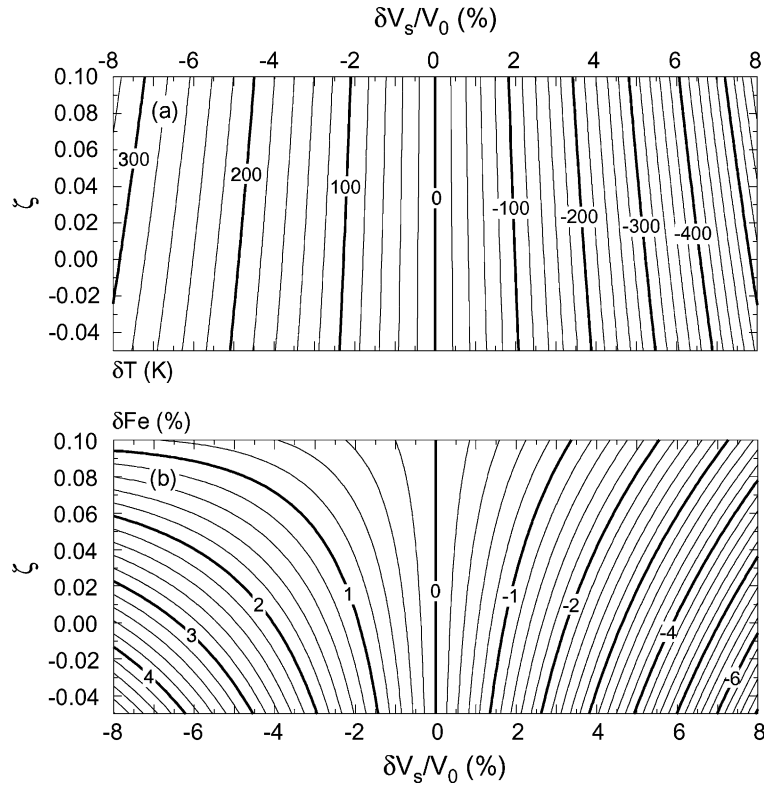


Fig. 4. Inversions of relative V_s -anomalies ($\delta V_s/V_0$) and scaling factor (ζ) for temperature anomalies of temperature (a) and iron ratio (b). The anomalies plotted here are the mean of the anomalies obtained for reference temperatures (T_{ref}) and olivine fraction ($X_{ol,ref}$) that predict reference velocity within $\pm 2.5\%$ of PREM (see text). The reference iron ratio is fixed and equal to 11%. Calculation were conducted for $z = 200$ km-depth.

using coefficients A , B , C and D Eq. (8) obtained for several reference temperatures (T_{ref}) and olivine fractions ($X_{ol,ref}$). The reference iron ratio is fixed and equal to 11%. We only kept the cases corresponding to the thermal and compositional reference models (T_{ref} and $X_{ol,ref}$) that could predict PREM within $\pm 2.5\%$. This results in mean distributions of δT and δFe with error bars of about 10% around the mean values.

As discussed in the Section 4.2, the distributions of δT and δFe are correlated to the distribution of the relative V_s -anomalies. Down to $z = 150$ km, continental cratons and platforms are colder than average and depleted in iron. Tectonically active areas and oceans are slightly hotter than average and enriched in iron. The correlation with surface tectonics holds down to 200 km, although the amplitudes of δT and δFe are smaller. At $z = 250$ km and $z = 300$ km, the

correlation with surface tectonics is much weaker and the amplitudes are smaller again. However, negative anomalies of temperature and depletion in iron are still present below cratons and stable platforms.

To quantify the correlation with surface tectonics, we have computed the mean of and the variance in the anomalies of temperature and iron for several regions (oceans, old cratons, stable platforms and tectonic continents as delimited by 3SMAC (Nataf and Ricard, 1996)) and depths. We first checked that, for the whole Earth, the mean anomalies of temperature and iron are close to zero, whatever the depth. For instance, the mean anomalies of iron (temperature) is $\delta Fe = -0.1\%$ ($\delta T = -20$ K) at $z = 150$ km, and $\delta Fe = -0.04\%$ ($\delta T = -3$ K) at $z = 300$ km. The mean of and variance in temperature anomalies for different provinces and depths are displayed in Fig. 5,

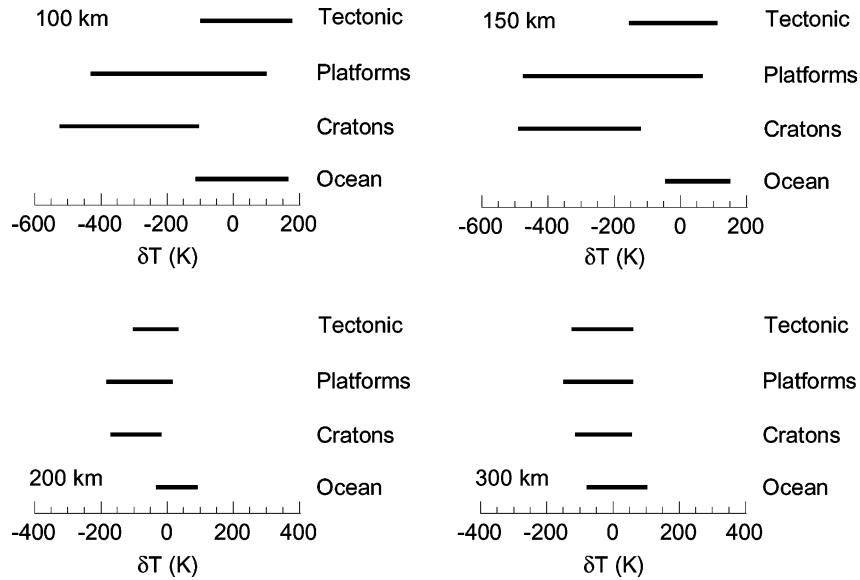


Fig. 5. Statistics on the distribution of temperature anomalies for several regions and depths (indicated on each plot). The tectonic regions are delimited following the model 3SMAC (Nataf and Ricard, 1996).

where each horizontal bar covers the interval $\overline{\delta T} + \sigma_{\delta T}$. Iron anomalies (Fig. 6) reveal a similar pattern. At shallow depths ($z < 200$ km), the distribution of temperature anomalies strongly depends on the

observed surface tectonics. Old cratons yield low mean anomalies of temperature and iron ($\overline{\delta T} \sim -310$ K and $\overline{\delta Fe} \sim -3.0\%$) with variances close to $\sigma_{\delta T} = 200$ K and $\sigma_{\delta Fe} = 2.0\%$, respectively. Compared to the

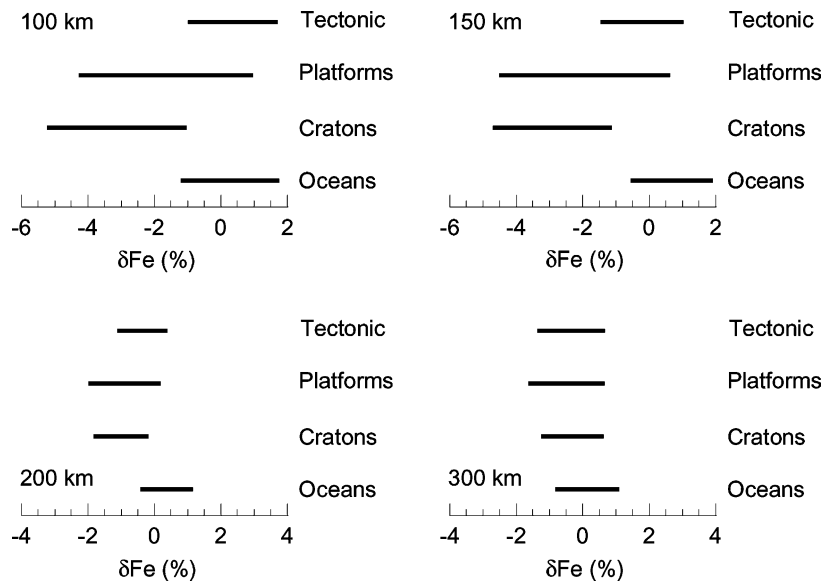


Fig. 6. Statistics on the distribution of iron anomalies for several regions and depths (indicated on each plot). The tectonic regions are delimited following the model 3SMAC (Nataf and Ricard, 1996).

average mantle, old cratons are, therefore, significantly colder and depleted in iron. This feature holds to a lesser extent for stable platforms, which yield higher mean anomalies ($\overline{\delta T} \sim -160$ K and $\overline{\delta Fe} \sim -1.7\%$) and variances ($\sigma_{\delta T} \sim 260$ K and $\sigma_{\delta Fe} \sim 2.6\%$) than old cratons. Oceans and tectonic continents, on the other hand, are more homogeneous. For these regions, the mean temperature and iron anomalies are close to zero and the variances are smaller ($\sigma_{\delta T} \sim 130$ K and $\sigma_{\delta Fe} \sim 1.4\%$), and therefore, there is no significant increase of temperature and/or enrichment in iron. At $z = 150$ km, oceans seem slightly warmer than the average mantle ($\overline{\delta T} \sim 50$ K), but the variance ($\sigma_{\delta T} \sim 90$ K) still suggests that it is not significant. At $z = 200$ km, the differences between tectonic regions is strongly damped. Old cratons remain slightly colder than the average mantle ($\overline{\delta T} \sim -90$ K and $\sigma_{\delta T} \sim 70$ K) and depleted in iron ($\overline{\delta Fe} \sim -1.0\%$ and $\sigma_{\delta Fe} \sim 0.8\%$). Anomalies of temperature and iron in stable platforms are now very similar to those observed in old cratons. Tectonic continents are slightly colder and depleted in iron than average, whereas oceans are slightly warmer and enriched in iron. Finally, at $z = 300$ km the distributions of temperature and iron anomalies are homogeneous and do not depend on the surface tectonics. Whatever the region, iron (temperature) anomalies are centered on $\overline{\delta Fe} = 0$ ($\overline{\delta T} = 0$) with a variance close to $\sigma_{\delta Fe} = 0.9\%$ ($\sigma_{\delta T} = 90$ K).

The results presented in this paper agree with the recent study of Forte and Perry (2000), who found anomalies of temperature and iron of $\delta T = -400$ K and $\delta Fe = -2\%$ in continental roots. Forte and Perry (2000) used a method similar to that presented in this paper. A major difference is that they used several geodynamic data sets, including surface dynamic topography, to constrain the density and to compute the scaling factor. In this study, we constrained density with gravity anomalies only. Although dynamic topography is important to constrain the density structure of the upper mantle, the conversion from observed to dynamic topography is very delicate, and we decided to omit it. Another difference is that we used a refined numerical model to invert relative V_s -anomalies and ζ for δT and δFe (Section 4.1 and Appendix A).

The important conclusion of Figs. 5 and 6 is that seismic and gravity data are explained by simultaneous anomalies of temperature and iron content. The

regions where the material is colder than average are also depleted in iron. In other words, the increase of density due to temperature drop is lowered by a lack of iron. Depending on their respective amplitudes, the depletion in iron may balance the cooling of the continents and play an important role in the stability of continental platforms and cratons. We discuss this point in details in Section 5.

4.5. An additional test

The scaling factor was constructed from gravity and S-wave velocity anomalies. We then determine anomalies of temperature and iron by inverting the V_s -correlated density anomalies and the V_s -anomalies. We omitted the density information uncorrelated to V_s , which may lead to small biases. For instance, our inferred anomalies of temperature and iron remain perfectly correlated to V_s -anomalies, as mentioned in Section 4.3. It would be more appropriate to introduce another independent data set, such as P-wave velocity anomalies. However, few studies provide V_p -anomalies in the upper mantle. In replacement, one can use S and P travel time residuals (δt_s and δt_p). The ratio $a = \delta t_s / \delta t_p$ is related to the ratio χ of the relative variations of V_p to the relative variations of V_s :

$$\chi = \frac{\partial \ln V_p}{\partial \ln V_s} = \frac{1}{a} \frac{V_{p,\text{ref}}}{V_{s,\text{ref}}} \quad (10)$$

where $V_{p,\text{ref}}$ and $V_{s,\text{ref}}$ are the reference P- and S-waves velocities. For the upper mantle Robertson and Woodhouse (1997) have found $a = 2.85 \pm 0.19$, independently of the tectonic region. For North America, Vinnik et al. (1999) proposed values of a between 3.49 and 3.97. We used this additional constraint to test our results. Following the method of Vacher et al. (1998), we computed the relative anomalies of P-wave predicted by our distributions of δT and δFe . We then obtained values of χ according to Eq. (10), and convert χ into a using PREM (Dziewonski and Anderson, 1981). For the whole Earth, we find $a = 2.78 \pm 0.4$ at $z = 100$ km, and $a = 3.14 \pm 0.2$ at $z = 200$ km depth. For North America, $a = 2.70 \pm 0.4$ at $z = 100$ km, and $a = 3.10 \pm 0.2$ at $z = 200$ km depth. These values are in good agreement with Robertson and Woodhouse (1997) and, to a lesser extent, with Vinnik et al. (1999).

5. Dynamic implications

5.1. Stability analysis

We now perform a stability analysis in the case of a layer submitted to chemical and thermal buoyancy. Chemical buoyancy is driven by anomalies of density $\delta\rho_c$ that result from compositional anomalies located in a root of thickness d_r and length l_r . Thermal buoyancy is driven by anomalies of density resulting from temperature anomalies $\delta\rho_{th} = -\alpha\rho_0\delta T$ (where α is thermal expansion), located in a thermal boundary layer (TBL) of mean thickness δ and length L (this length is also the length of the convective cell). As proposed by Lenardic and Moresi (1999), the characteristic lengths of the problem, which will be used to non-dimensionalize the equations, are the depth of the mantle D and the length of a convective cell L . The parameter $B = -\delta\rho_c/\delta\rho_{th}$ is known as the buoyancy ratio. The deviation from hydrostatic equilibrium induced by the density anomalies $\delta\rho_{th}$ and $\delta\rho_c$ is given by the pressure P :

$$P = (d_r l_r \delta\rho_c - \delta L \alpha\rho_0 \delta T) \frac{g}{L} \quad (11)$$

where g is the acceleration of gravity.

If the term in parenthesis in Eq. (11) is negative, the root is buoyant and does not sink. This corresponds to the third regime defined by Lenardic and Moresi (1999).

Introducing the buoyancy ratio B , and using non-dimensional variables ($l'_r = l_r/L$, $d'_r = d_r/D$ and $\delta' = \delta/D$), one gets a condition for this regime:

$$B > \frac{\delta'}{d'_r l'_r} \quad (12)$$

This condition is the same as Eq. (7) of Lenardic and Moresi (1999) and is valid for negative anomalies of temperature (i.e. $\delta\rho_{th} > 0$) only. Typical values for d_r and l_r are 300 and 1000 km, respectively. Assuming $D \sim 3000$ km (in case of whole mantle convection) and $L \sim 2000$ km, the condition (12) implies that $B > 20\delta'$. For instance, if $B = 1$ the negative buoyancy induced by a 150 km ($\delta' = 0.05$, if one considers whole mantle convection) thick TBL is balanced. If the term in parenthesis in Eq. (11) is positive, the material will sink, with a velocity u_z . However, friction forces

inhibit this motion and favor buoyancy. The frictional force per unit of surface (f) is approximated by

$$f \sim Au_z \frac{\mu}{d_r} \quad (13)$$

where A is a constant, and μ the viscosity of the material. The velocity u_z can be scaled according to the physical properties of the system. Usually, velocity is scaled by the ratio of the thermal diffusivity (κ) to the depth of the system (here the depth of the root), and

$$f \sim A' \frac{\mu\kappa}{d_r^2} \quad (14)$$

where A' is a dimensionless constant. Motion occurs when P is greater than f (in absolute value). At the onset, the buoyancy ratio is such that

$$B_c = \frac{\delta'}{d'_r l'_r} + \frac{C}{\delta T' d_r'^3 l_r'}, \quad C = \frac{A'}{Ra},$$

$$Ra = \frac{\alpha\rho_0 g \Delta T D^3}{\mu\kappa}. \quad (15)$$

In this equation Ra is the Rayleigh number, ΔT the non-adiabatic temperature difference across the mantle, and $\delta T' = \delta T/\Delta T$. If the buoyancy ratio is greater (smaller) than B_c , the root is stable (sinks). The conditions to create a buoyant root are easier to satisfy as the value of B_c is smaller. A difficulty is to estimate the value of A' . Friction increases with the value of A' (Eq. (14)), which may depend on the rheology of the fluid and/or on the type of boundary condition at the surface. For instance, one expects that A' increases with the strength of the rock (i.e. for harder rheologies). Stability analysis for purely thermal convection (e.g. Sotin and Labrosse, 1999), defines A' as the TBL Rayleigh number (Ra_δ). In the case of an isoviscous fluid with free slip boundaries, studies showed that Ra_δ is roughly constant and equal to 6 for both top and bottom TBLs (Sotin and Labrosse, 1999). If one considers variable viscosity convection, or rigid boundary condition at the surface, the top TBL gets less unstable, and its Rayleigh number yields values around 100 (Deschamps and Sotin, 2000). Considering values of A' between 1 and 100, and Rayleigh numbers between 5×10^5 and 10^7 , one gets values of C between 10^{-7} and 5×10^{-3} . Fig. 7 represents B_c as a function of the absolute value of $\delta T'$ and for several values of $r' = \delta'/d'_r l'_r$ and C . For a

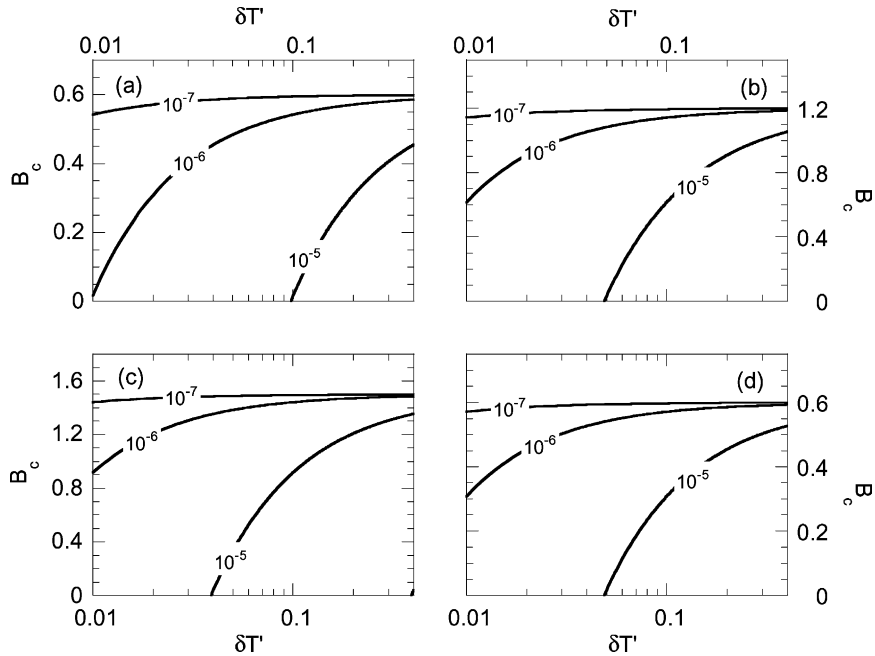


Fig. 7. Buoyancy ratio at the onset of instability (B_c) as a function of the absolute value of non-dimensional temperature anomalies ($\delta T'$) and for several values of $C = A'/Ra$. The ratio of the TBL thickness to the root thickness is $r' = 0.3$ (a), $r' = 0.6$ (b and d) and $r' = 0.75$ (c). The length of the root is $l'_r = 0.5$ (plots a to c) and $l'_r = 1.0$ (plot d).

given value of C , B_c decreases as r' increases (Fig. 7a and c). The stability of the root increases as the root is thicker and/or the TBL is thinner. In addition, the stability of the root increases with the length of the root (compare Fig. 7b and d). Finally, the parameter C has a strong influence on B_c . For given temperature anomaly and Rayleigh number, B_c gets significantly smaller as A' increases. As expected, rheology may play an important role in the stability of the layer.

5.2. Continental roots

A possible origin for the high-velocity anomalies observed in continental roots is that the constitutive material of these roots is simultaneously colder than the average mantle and depleted in iron (Section 4.4). This result has important consequences, since negative anomalies of density induced by low temperature would be balanced by positive anomalies of density induced by the depletion in iron. In other words, depletion in iron would prevent lateral and vertical flow due to the low temperatures of the root and explain

the stability of old cratons. To test this hypothesis, we have computed buoyancy ratios associated with the observed continental roots.

First, at a given depth we compute the anomalies of density, respectively induced by the inverted anomalies of temperature and iron. These anomalies of density are then integrated over depth, resulting in mean thermal ($\overline{\delta\rho_{th}}$) and compositional ($\overline{\delta\rho_c}$) density anomalies. At each location, the buoyancy ratio is finally given by $B = -\overline{\delta\rho_c}/\overline{\delta\rho_{th}}$. The error on B due to the uncertainties on the reference temperature is around 10%. Histograms in Fig. 8 represent the frequency of B (i.e. the ratio of the surface having a given value of B to the total surface) for old cratons (Fig. 8a and c) and stable platforms (Fig. 8b and d). Two thicknesses of the root (h_r) are considered: $h_r = 100$ km (Fig. 8a and b) and $h_r = 200$ km (Fig. 8c and d). The buoyancy ratio is centered on $B \sim 0.82$ for $h_r = 100$ km, and $B \sim 0.85$ for $h_r = 200$ km. In every case the dispersion is very small: the buoyancy ratio yields within 0.7 and 0.9 for more than 90% of the total surface of the root. These estimates are in good agreement

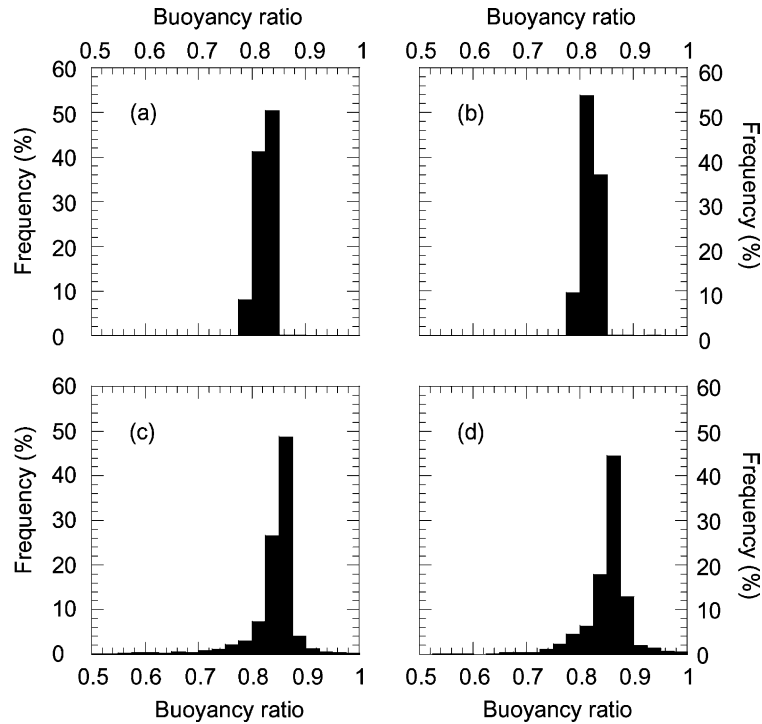


Fig. 8. Buoyancy ratio (B) in old cratons (a and c) stable platforms (b and d). The y-axis represent the percentage of the total surface of the root (or frequency) having a buoyancy ratio equal to a given value of B . The thickness of the root is equal to 100 km (a and b) or 200 km (c and d).

with those of Forte and Perry (2000), who found a buoyancy ratio close to 0.8. Note that the dispersion is higher in stable platforms than in old cratons, and that it increases slightly with the thickness of the root.

To compare these results with those of the stability analysis, one must chose values for ΔT , D and Ra . Different values may be considered, depending on the mode of mantle convection. The temperature at the 660 km discontinuity is relatively well constrained from mineral physics experiments. In the case of layered mantle convection, one may, therefore, chose the value of ΔT around 1600 K. In addition, $D = 660$ km and a typical value of the Rayleigh number is $Ra = 5.0 \times 10^5$. In the case of whole mantle convection $D = 2890$ km and the Rayleigh number is close to 10^7 . The temperature at the core–mantle boundary, on the other hand, is poorly constrained. A median value is $T_{\text{CMB}} = 3500$ K (including the adiabatic contribution) (e.g. Williams, 1998). Assuming that the adiabatic increase of temperature across the

whole mantle is about 1000 K this estimate leads to $\Delta T \sim 2500$ K. Typical values for the anomalies of temperature below cratons are $\delta T = -330 \pm 200$ K (see Section 4.4). For whole mantle (layered) convection values of $\delta T'$ in old cratons yield between -0.05 and -0.2 (-0.08 and -0.3). To estimate the non-dimensional parameter C , we assumed that A' varies between 1 (for soft rheology) and 100 (for hard rheology). Therefore, $10^{-7} \leq C \leq 10^{-5}$ for whole mantle convection, and $2 \times 10^{-6} \leq C \leq 2 \times 10^{-4}$ for layered convection. Other scaling are reported in Table 1 for whole mantle and layered convection.

TBLs transfer heat by conduction. An estimate of the thickness of the TBL at the top of the mantle is, therefore,

$$\delta = k \frac{\Delta T_e}{q_m} \quad (16)$$

where k is the thermal conductivity of the rock, ΔT_e the temperature difference across the TBL, and q_m

Table 1
Scaling of the parameters used in stability analysis

Parameter	Typical values (dimensional)	Symbol	Whole mantle convection	Layered convection
Temperature anomaly ^a	100–500 K	$\delta T'$	0.04–0.2	0.06–0.3
TBL thickness	75–270 km ^b	δ'	0.03–0.09	0.1–0.4
–	10–60 km ^c	–	3×10^{-3} –0.02	0.02–0.09
Root thickness	100–300 km	d'	0.04–0.1	0.15–0.45
Root length	1000–2000 km	l'	0.5–1.0	0.5–1.0
A'/Ra^d		C	10^{-7} to 10^{-5}	2×10^{-6} to 2×10^{-4}

^a Absolute values.

^b Case of an isoviscous mantle (see text).

^c Case of a strongly temperature-dependent mantle viscosity (see text).

^d A' is a parameter that depends on the rheology and Ra is the Rayleigh number. Higher values of A' (and, therefore, of C) are obtained for harder rheologies (e.g. strongly temperature-dependent mantle viscosity).

the heat flux at the top of the TBL. This heat flow can be estimated by removing the crustal heat production from the surface heat flow. For cratonic areas, Jaupart and Mareschal (1999) estimated q_m around 10–15 mW/m² (Canadian shield) and 17 mW/m² (South Africa). Studies of experimental and numerical convection have shown that the thickness of the TBL (and, therefore, the temperature difference across this layer) depends on the fluid rheology, and particularly on the properties of the fluid viscosity (e.g. Richter et al., 1983; Davaille and Jaupart, 1993; Moresi and Solomatov, 1995). If the viscosity does not depend on temperature, all the fluid participates in the flow and the top TBL can be safely approximated by the conductive layer that lies at the top of the fluid. Assuming that the temperature at the top of the mantle (around $z = 50$ km depth) is close to 700 K and that the mantle adiabat yields between 1200 and 1600 K, one gets $500 \leq \Delta T_e \leq 800$ K. For $k = 3$ W/m/K and $10 \leq q_m \leq 20$ mW/m², the thickness of TBL is between 75 and 270 km (see Table 1 for non-dimensional values). These values constitute an upper bound. Indeed, if the fluid viscosity is strongly temperature-dependent, a viscous lid develops at the top of the fluid. This layer is stable and it does not participate to convection. It transfers heat by conduction with a heat flux equal to that of the TBL. To estimate the thickness of the TBL, one must remove the stable layer from the top conductive layer. Davaille and Jaupart (1993) proposed that ΔT_e is proportional to a “viscous temperature scale” ΔT_v . Following this result and assuming an Arrhenius type

of law for the viscosity of the rock, one gets

$$\Delta T_e = 2.24 \frac{RT_m^2}{Q} \quad (17)$$

where R is the gas constant, Q the activation energy of the rock, and T_m is the mean adiabatic temperature of the mantle. Taking $2.4 \times 10^5 \leq Q \leq 4.3 \times 10^5$ kJ/mol (e.g. Karato and Wu, 1993) and $1200 \text{ K} \leq T_m \leq 1600 \text{ K}$, one finds $60 \text{ K} \leq \Delta T_e \leq 200 \text{ K}$. If $k = 3$ W/m/K and $10 \leq q_m \leq 20$ mW/m², the thickness of the TBL yields between 10 and 60 km (see Table 1 for non-dimensional values). These estimates are significantly lower than those for constant viscosity.

According to Fig. 7, the continental root is more stable if viscosity is strongly temperature-dependent. In that case, the value of C is higher (i.e. the frictions are larger), and the TBL is thinner than in the case of a constant viscosity. For cratons and stable platforms (Fig. 8), the buoyancy ratio is close to $B = 0.8 \pm 0.2$ (this error bar includes dispersion on B and uncertainty due to possible errors on the reference temperature and on the V_s -anomalies). In the case of temperature-dependent viscosity, $\delta \leq 50$ km and if the thickness (d) of the root is equal to 200 km, the ratio $r' = \delta/d$ is lower than 0.3. The value of B for cratons and platforms is clearly higher than the critical buoyancy ratio for $r' = 0.3$, even for low values of C (Fig. 7a). In other words, the negative buoyancy induced by low temperature is completely balanced and the root is stable. If the thickness of the root and of the TBL are equal to 100 and 60 km, respectively, $r' = 0.6$ and one needs values of C around 2×10^{-5} to keep the

root stable (Fig. 7b). This condition is easier to satisfy in the case of layered convection ($A' \sim 10$) than in the case of whole mantle convection ($A' \sim 200$). The case $\delta = 100$ and 60 km is, however, a limit case. First continental roots are present down to 250–300 km. And second, $\delta = 60$ km is an upper bound if one considers a strongly temperature-dependent viscosity. In the case of constant (or slightly temperature-dependent) viscosity, the TBL is likely thicker than 75 km and A' less than 10. For a 200 km-root and small values of the TBL thickness ($75 \leq \delta \leq 100$), $0.375 \leq r' \leq 0.5$ and there is no clear conclusions. In the case of whole mantle convection, on the other hand, C has values higher than 10^{-6} and the root is likely unstable. Note that the opposite conclusion cannot be excluded if one considers large roots ($l'_r = 1.0$) (Fig. 7d). Finally, if the TBL is thicker than $\delta = 100$ km, or if the root is thinner than $d = 200$ km, it is reasonable to think that the root is not stable, whatever the mode of mantle convection (Fig. 7c).

6. Discussion and conclusions

Regions of high positive V_s -anomalies extend down to 250–300 km below old cratons and stable platforms, and are interpreted as chemically distinct mantle, or tectosphere. Previous studies based on seismological observations proposed that the tectosphere is indeed depleted in iron (e.g. Jordan, 1988; Anderson, 1990; Polet and Anderson, 1995). However, because seismic velocities are also sensitive to temperatures, no clear cut conclusions can be made from seismic data only. An alternative is to invert geodynamic data sets (e.g. gravity anomalies) for anomalies of temperature and composition (Forte and Perry, 2000; this study). Such studies support the hypothesis that continental roots are strongly depleted in iron. An important conclusion of the present study is that the relative density-to-shear wave velocity ratio (ζ) is such that temperature anomalies alone cannot be responsible for the observed V_s -anomalies and ζ . Simultaneous variations of iron and temperature are required to explain gravity and seismic velocity anomalies. Regions that are colder (warmer) than the average mantle are also depleted (enriched in iron). For instance, below cratons the mean anomalies of temperature and iron are close to -330 K and -3.2% , respectively.

Polet and Anderson (1995) found that the extent of continental roots is strongly correlated to the age of cratons, the Archean cratons having the deepest roots. A current hypothesis is that present day cratonic roots result from an intense volcanic activity at the Archean (e.g. Herzberg, 1993; Polet and Anderson, 1995; and references therein). The melts extracted from a pyrolite source are enriched in CaO, Al_2O_3 and FeO, resulting in a depleted continental uppermost mantle.

It has been proposed that the negative buoyancy induced by temperatures lower than average are balanced by positive buoyancy due to depletion in iron (e.g. Jordan, 1975, 1988; Forte et al., 1995). However, rheology also plays an important role in the stability of roots. Numerical models including both temperature-dependent viscosity and chemical differentiation due to partial melting (deSmet et al., 1999) have shown that the layered structure resulting from differentiation remains stable over a long period of time (≥ 1.0 Gyr). Using simple physical laws, Lenardic and Moresi (1999) concluded that buoyancy alone cannot stabilize the continental roots. In addition to buoyancy, the mantle viscosity must be strongly temperature-dependent. Our stability analysis is in good agreement with this conclusion, although the value of A' as a function of the rheology is not well constrained. There is, however, a serious restriction in invoking temperature-dependent viscosity: to be consistent, one must assume a temperature-dependent viscosity throughout the whole uppermost mantle (and not only below cratons), which would inhibit plate tectonics (Lenardic and Moresi, 1999). This difficulty can be solved assuming that the cratonic mantle is poor in volatiles. Indeed, Polet and Anderson (1995) noted that cratonic Archean mantle could have been dried out by high-temperature melt extraction. Creep flow laws are significantly different whether the environment is wet or dry, and drier materials have higher strengths (e.g. Karato and Wu, 1993; Mackwell et al., 1998). Therefore, if volatiles have been massively extracted from the continental uppermost mantle during the Archean, old cratons would be difficult to deform, and they would remain stable over long periods of time.

A major concern of this study was to estimate the error bars on the temperature and iron anomalies. These error bars reach 10%, excluding errors induced by the uncertainties on V_s -anomalies. Refined models

of seismic tomography models, including error bars, and a better knowledge of the mantle adiabat would reduce uncertainties on inverted temperature and iron anomalies. Another improvement would be to account for the rheology more accurately, including the role and influence of volatiles. Stability analysis suggests that roots are stable only if the mantle viscosity is strongly temperature-dependent. However, the stability of the top TBL for a fluid including temperature-dependent viscosity and chemical roots is not well understood. Systematic studies of numerical or experimental convection should be conducted to determine criteria of stability as a function of rheology and chemical differentiation.

Acknowledgements

We thank Pierre Vacher who provided us the original version of the software computing synthetic densities and seismic velocities from temperature and mineralogical composition. We are also grateful to two anonymous reviewers for their useful comments. This research was partly funded by the Netherlands Organization for Scientific Research (NWO, grant 750.297.02).

Appendix A. Computation of density and seismic velocities

Numerical models can predict densities and seismic velocities in the mantle, for a given thermodynamic state (temperature and pressure) and a given petrology. In this study, we have used a numerical method based on Grüneisen's and adiabatic finite strain theories (e.g. Duffy and Anderson, 1989; Vacher et al., 1996). Densities and elastic moduli of individual minerals at ambient temperature and pressure are first projected at temperature T and pressure p . The density and elastic moduli of the rock are then obtained by averaging the individual densities and elastic moduli as a function of the petrologic model.

The density and the elastic parameter of each mineral at temperature T are obtained from Grüneisen's theory:

$$\rho(T, p = 0) = \rho_0 \exp \left[- \int_{T_0}^T \alpha(T') dT' \right], \quad (\text{A.1})$$

$$M(T, p = 0) = M_0 \left[\frac{\rho(T)}{\rho_0} \right]^{\beta_M},$$

$$\beta_M = - \frac{1}{\alpha_0 M_0} \left(\frac{\partial M}{\partial T} \right)_p, \quad (\text{A.2})$$

where M stands for the bulk (K) or shear (G) modulus and the subscript "0" indicates values of the parameter at ambient temperature (T_0) and pressure ($p = 0$). The temperature dependence of the thermal expansion α is well described by

$$\alpha(T) = a_1 + a_2 T - \frac{a_3}{T^2} + \frac{a_4}{T}, \quad (\text{A.3})$$

where the coefficient a_i are deduced from laboratory experiments (Table 2).

The density and elastic moduli are then projected at depth following a Birch–Murnaghan adiabatic compression to the third order:

$$p = -3K_{T,0}(1 - 2\varepsilon)^{5/2}(\varepsilon + \frac{1}{2}B\varepsilon^2),$$

$$B = 3K \left[4 - \left(\frac{\partial K}{\partial p} \right)_T \right], \quad (\text{A.4})$$

where ε is the strain of the mineral. For a given pressure, Eq. (A.4) is solved for the strain. The density, bulk and shear moduli at temperature T and pressure p are then, respectively given by

$$\rho(T, p) = \rho_{T,0}(1 - 2\varepsilon)^{3/2} \quad (\text{A.5})$$

$$K(T, p) = (1 - 2\varepsilon)^{5/2}(K_{T,0} + C_K \varepsilon),$$

$$C_K = 5K_{T,0} - 3K_{T,0} \left(\frac{\partial K}{\partial p} \right)_T, \quad (\text{A.6})$$

Table 2
Thermal expansion of some minerals^a

Mineral	a_1 (10^{-5} K^{-1})	a_2 (10^{-8} K^{-2})	a_3 (K)	a_4 (10^{-2})
Olivine	2.832	0.758	0	0
Diopside	3.206	0.811	1.8167	0.1347
Enstatite	2.860	0.720	0	0
Garnet	2.810	0.316	0.4587	0
Jadeite	2.560	0.260	0	0

^a Thermal expansion is computed following Eq. (A.3). Compilation is after Vacher et al. (1998). See references of experimental studies therein.

Table 3
Densities and elastic properties of some minerals^a

Mineral	X ^b (%)	ρ_0 (g/cm ³)	K_0 (GPa)	$\partial K/\partial p$	$\partial K/\partial T$ (GPa/K)	G_0 (GPa)	$\partial G/\partial p$	$\partial G/\partial T$ (GPa/K)
Olivine	61.7	3.222 + 1.182xFe	128	4.3	-0.016	81 - 30xFe	1.4	-0.014
Diopside	13.3	3.277 + 0.38xFe	105 + 13xFe	6.2 - 1.9xFe	-0.013	67 - 6xFe	1.7	-0.010
Enstatite	5.2	3.215 + 0.799xFe	124	5.6	-0.012	78 - 24xFe	1.4	-0.011
Garnet	15.3	3.565 + 0.76xFe	173 + 7xFe	5.3	-0.021	92 + 7xFe	2.0	-0.010
Jadeite	4.5	3.320	126	5.0	-0.016	84	1.7	-0.013

^a Compilation is after Vacher et al. (1998). See references of experimental studies therein.

^b Volumic fraction in pyrolite.

$$G(T, p) = (1 - 2\varepsilon)^{5/2}(G_{T,0} + C_G\varepsilon),$$

$$C_G = 5G_{T,0} - 3K_{T,0} \left(\frac{\partial G}{\partial p} \right)_T. \quad (\text{A.7})$$

The subscript “T,0” denotes the values of the parameter at temperature T and zero pressure. Values of the elastic moduli at ambient condition, and their derivatives with respect to pressure and temperature are reported in Table 3.

The temperature at the foot of the adiabat must also be projected at depth. The increment of temperature due to the increase of pressure is controlled by the adiabatic gradient of temperature γ_S , and the end (or real temperature) is given by

$$T_f = T + \gamma_S(p - p_0),$$

$$\gamma_S = \left(\frac{\partial T}{\partial p} \right)_S = \left(\frac{\alpha T}{\rho C_p} \right)_{p,T} \left(\frac{\rho_0}{\rho} \right)^{6.5} \quad (\text{A.8})$$

Knowing the end-temperature, one can estimate the sensitivity of density and seismic velocities to temperature.

Densities and elastic moduli of individual minerals depend on the volumic fraction of iron, i.e. the ratio $x\text{Fe} = \text{Fe}/(\text{Fe} + \text{Mg})$. The method used in this paper accounts for this dependence. For each mineral, and prior to projection at temperature T and pressure p , the density and elastic moduli at ambient temperature and pressure are corrected as indicated in Table 3. One can, therefore, estimate the sensitivity of density and seismic velocities to the iron content. The properties of the rock assemblage are computed from the properties of individual minerals according a petrologic model. Considering different petrologic models, one can estimate the sensitivity of density

and seismic velocities to compositional variations (e.g. variations in the volumic fraction of olivine). In this study, we only considered the minerals present in the uppermost mantle (Table 3). The density of the rock ($\bar{\rho}$) is simply the volumetric average of the densities of the minerals composing the rock. The bulk and shear modulus (\bar{K} and \bar{G}) are computed following the Hashin–Shtrickman averaging, which is well suited for the upper mantle (Vacher et al., 1996). Finally, the P-wave and S-wave velocity of the rock are given by

$$V_p = \sqrt{\frac{\bar{K} + (4/3)\bar{G}}{\bar{\rho}}} \quad \text{and} \quad V_s = \sqrt{\frac{\bar{G}}{\bar{\rho}}}. \quad (\text{A.9})$$

References

- Alsina, D., Woodward, R.L., Snieder, R.K., 1996. Shear wave velocity structure in North America from large-scale waveform inversions of surface waves. *J. Geophys. Res.* 101, 15969–15986.
- Anderson, D.L., 1987. Thermally induced phase changes, lateral heterogeneity of the mantle, continental roots, and deep slab anomalies. *J. Geophys. Res.* 92, 13968–13980.
- Anderson, D.L., 1990. Geophysics of the continental mantle: an historical perspective. In: M. Menzies (Ed.) *Continental Mantle*. Clarendon Press, Oxford, pp. 1–30.
- Anderson, D.L., Given, J.W., 1982. Absorption band Q model for the Earth. *J. Geophys. Res.* 87, 3893–3904.
- Davaille, A., Jaupart, C., 1993. Transient high Rayleigh number thermal convection with large viscosity variations. *J. Fluid Mech.* 253, 141–166.
- Davies, G.F., Dziewonski, A.M., 1975. Homogeneity and constitution of the Earth’s lower mantle and outer core. *Phys. Earth Planet Inter.* 10, 336–343.
- Deschamps, F., Sotin, C., 2000. Inversion of two-dimensional numerical convection experiments for a fluid with a strongly temperature-dependent viscosity. *Geophys. J. Int.* 143, 204–218.

- Deschamps, F., Snieder, R., Trampert, J., 2001. The relative density-to-shear velocity scaling in the uppermost mantle. *Phys. Earth Planet. Inter.* 124, 193–211.
- deSmet, J.H., van den Berg, A.P., Vlaar, N.J., 1999. The evolution of continental roots in numerical thermo-chemical mantle convection models including differentiation by partial melting. *Lithos* 48, 153–170.
- Doin, M.-P., Fleitout, L., McKenzie, D., 1996. Geoid anomalies and the structure of continental and oceanic lithospheres. *J. Geophys. Res.* 101, 16119–16135.
- Duffy, T.S., Anderson, D.L., 1989. Seismic wave speeds in mantle minerals and the mineralogy of the upper mantle. *J. Geophys. Res.* 94, 1895–1912.
- Dziewonski, A.M., Anderson, D.L., 1981. Preliminary reference earth model. *Phys. Earth Planet. Inter.* 25, 297–356.
- Forte, A.M., Peltier, W.R., 1991. Viscous flow models of global geophysical observables. I. Forward problems. *J. Geophys. Res.* 96, 20131–20159.
- Forte, A.M., Perry, A.C., 2000. Seismic-geodynamic evidence for a chemically depleted continental tectosphere. *Science* 290, 1940–1944.
- Forte, A.M., Dziewonski, A.M., O'Connell, R.J., 1995. Thermal and chemical heterogeneity in the mantle: a seismic and geodynamic study of continental roots. *Phys. Earth Planet. Inter.* 92, 45–55.
- Goes, S., Govers, R., Vacher, P., 2000. Shallow mantle temperatures under Europe from P- and S-wave, tomography. *J. Geophys. Res.* 105, 11153–11169.
- Herzberg, C.T., 1993. Lithosphere peridotites of the Kaapvaal craton. *Earth Planet. Sci. Lett.* 120, 13–29.
- Jackson, A., 2000. Laboratory measurement of seismic wave dispersion and attenuation: recent progress. In: Karato, S.I., Forte, A.M., Lieberman, R.C., Masters, G., Stixrude, L. (Eds.), *Earth's Deep Interior: Mineral Physics and Tomography from the Atomic to the Global Scale*, Geophys. Monogr. Ser., Vol. 117., American Geophysical Union, Washington, DC, pp. 3–36.
- Jaupart, C., Mareschal, J.C., 1999. The thermal structure and thickness of continental roots. *Lithos* 48, 93–114.
- Jordan, T.H., 1975. The continental tectosphere. *Rev. Geophys. Space Phys.* 13, 1–12.
- Jordan, T.H., 1979. Mineralogies, densities and seismic velocities of garnet lherzolites and their geophysical implications. In: Boyd, F.R., Meyer, H.O.A. (Eds.), *The Mantle Sample: Inclusions in Kimberlites and Other Volcanics*. American Geophysical Union, Washington, DC, pp. 1–14.
- Jordan, T.H., 1988. Structure and formation of the continental tectosphere. *J. Petrol. (Special Lithosphere Issue)*, 11–37.
- Karato, S.-I., 1993. Importance of anelasticity in the interpretation of seismic tomography. *Geophys. Res. Lett.* 20, 1623–1626.
- Karato, S.-I., Wu, P., 1993. Rheology of the upper mantle: a synthesis. *Science* 260, 771–778.
- Kogan, M.K., McNutt, M.K., 1993. Gravity field over northern Eurasia and variations in the strength of the upper mantle. *Science* 259, 473–479.
- Lemoine, F.G., Kenyon, S.C., Factor, J.K., Trimmer, R.G., Pavlis, N.K., Chinn, D.S., Cox, C.M., Klosko, S.M., Luthcke, S.B., Torrence, M.H., Wang, Y.M., Williamson, R.G., Pavlis, E.C., Rapp, R.H., Olson, T.R., 1998. The Development of the Joint NASA GSFC and National Imagery Mapping Agency (NIMA) Geopotential Model EGM96. NASA/TP-1998-206861, NASA, GSFC, Greenbelt, MD, 20771.
- Lenardic, A., Moresi, L.-N., 1999. Some thoughts on the stability of cratonic lithosphere: effects of buoyancy and viscosity. *J. Geophys. Res.* 104, 12747–12758.
- Mackwell, S.J., Zimmerman, M.E., Kohlstedt, D.L., 1998. High-temperature deformation of dry diabase with applications to tectonics on Venus. *J. Geophys. Res.* 103, 975–984.
- Mégnin, C., Romanowicz, B., 2000. The three-dimensional shear velocity structure of the mantle from the inversion of body, surface and higher-mode waveforms. *Geophys. J. Int.* 143, 708–728.
- Minster, J.B., Anderson, D.L., 1981. A model of dislocation-controlled rheology for the mantle. *Philos. Trans. R. Soc. London* 299, 319–356.
- Mitrovica, J.X., Forte, A.M., 1997. Radial profile of mantle viscosity: results from the joint inversion of convection and post-glacial rebound observables. *J. Geophys. Res.* 102, 2751–2769.
- Moresi, L.-N., Solomatov, V.S., 1995. Numerical investigation of two-dimensional convection with extremely large viscosity variations. *Phys. Fluids* 7, 2154–2162.
- Nataf, H.-C., Ricard, Y., 1996. 3SMAC: an a priori tomographic model for upper mantle based on geophysical modeling. *Phys. Earth Planet. Inter.* 95, 101–122.
- Polet, J., Anderson, D.L., 1995. Depth extent of cratons as inferred from tomographic studies. *Geology* 23, 205–208.
- Richter, F.M., Nataf, H.C., Daly, S.F., 1983. Heat transfer and horizontally averaged temperature of convection with large viscosity variations. *J. Fluid Mech.* 129, 173–192.
- Ritsema, J., van Heijst, H., 2000. New seismic model of the upper mantle beneath Africa. *Geology* 28, 63–66.
- Robertson, G.S., Woodhouse, J.H., 1997. Comparison of P- and S-station corrections and their relationship to upper mantle structure. *J. Geophys. Res.* 102, 27355–27366.
- Sobolev, S.V., Zeyen, H., Stoll, G., Werling, F., Altherr, R., Fuchs, K., 1996. Upper mantle temperatures from teleseismic tomography of French Massif Central including effects of composition, mineral reaction, anharmonicity, anelasticity and partial melting. *Earth Planet. Sci. Lett.* 139, 147–163.
- Sotin, C., Labrosse, S., 1999. Three-dimensional thermal convection in an isoviscous, infinite Prandtl number fluid heated from within and from below: applications to the transfer of heat through planetary mantles. *Phys. Earth Planet. Inter.* 112, 171–190.
- Su, W.-J., Dziewonski, A.M., 1997. Simultaneous inversions for three-dimensional variations in shear and bulk velocity in the mantle. *Phys. Earth Planet. Inter.* 100, 135–156.
- Vacher, P., Mocquet, A., Sotin, C., 1996. Comparison between tomographic structures and models of convection in the upper mantle. *Geophys. J. Int.* 124, 45–56.
- Vacher, P., Mocquet, A., Sotin, C., 1998. Computation of seismic profiles from mineral physics: the importance of non-olivine components for explaining the 660 km depth discontinuity. *Phys. Earth Planet. Inter.* 106, 275–298.
- Villaseñor, A., Ritzwoller, M.H., Levshin, A.L., Barmin, M.P., Engdahl, E.R., Spakman, W., Trampert, J., 2001. Shear velocity

- structure of central Eurasia from inversion of surface wave velocities. *Phys. Earth Planet. Inter.* 123, 169–184.
- Vinnik, L., Chevrot, S., Montagner, J.P., Guyot, F., 1999. Teleseismic travel time residuals in North America and anelasticity of the asthenosphere. *Phys. Earth Planet. Inter.* 116, 93–103.
- Williams, Q., 1998. The temperature contrast across the D'' . In: Gurnis, M., Wysession, M.E., Knittle, E., Buffet, B.A. (Eds.), *The Core–Mantle Boundary Region*, Geodynamics Series, Vol. 28. American Geophysical Union, Washington, DC, pp. 73–81.
- Woodhouse, J.H., Trampert, J., 1995. Global upper mantle structure inferred from surface wave and body wave data. *EOS Trans. American Geophysical Union*, p. F422.